CONTRAST MEDIA & MOLECULAR IMAGING

Received: 7 September 2011, Revised: 15 July 2012, Accepted: 23 August 2012, Published online in Wiley Online Library:

(wileyonlinelibrary.com) DOI: 10.1002/cmmi.1502

A dual magnetic resonance imaging/fluorescent contrast agent for Cathepsin-D detection

Robert Ta[a,b], Mojmir Suchy[a,c], Joshua H.K. Tam[d,e], Alex X. Li[a], Francisco S. Martinez-Santiesteban[b], Timothy J. Scholl[a,b], Robert H.E. Hudson[c], Robert Bartha[a,b] and Stephen H. Pasternak[d,e,f]*

Currently there are no approved biomarkers for the pre-symptomatic diagnosis of Alzheimer's disease (AD). Cathepsin-D (Cat-D) is a lysosomal protease that is present at elevated levels in amyloid plaques and neurons in patients with AD and is also elevated in some cancers. We have developed a magnetic resonance imaging (MRI)/fluorescent contrast agent to detect Cat-D enzymatic activity. The purpose of this study was to investigate the cellular and tissue uptake of this MRI/fluorescent contrast agent. The agent consists of an MRI probe [DOTA–caged metal ion (Gd^{3+} or Tm^{3+})] and a fluorescent probe coupled to a cell-penetrating-peptide sequence by a Cat-D recognition site. The relaxivity of Gd^{3+}–DOTA–$CAT_{(cleaved)}$ was measured in 10% heat-treated bovine serum albumin (BSA) phantoms to assess contrast efficacy at magnetic fields ranging from 0.24 mT to 9.4 T. *In vitro*, Tm^{3+}–DOTA–CAT was added to neuronal SN56 cells over-expressing Cat-D and live-cell confocal microscopy was performed at 30 min. Tm^{3+}–DOTA–CAT was also intravenously injected into APP/PS1-dE9 Alzheimer's disease mice ($n = 9$) and controls ($n = 8$). Cortical and hippocampal uptake was quantified at 30, 60 and 120 min post-injection using confocal microscopy. The liver and kidneys were also evaluated for contrast agent uptake. The relaxivity of Gd^{3+}–DOTA–$CAT_{(cleaved)}$ was 3.3 $(mM\,s)^{-1}$ in 10% BSA at 9.4 T. *In vitro*, cells over-expressing Cat-D preferentially took up the contrast agent in a concentration-dependent manner. *In vivo*, the contrast agent effectively crossed the blood–brain barrier and exhibited a distinct time course of uptake and retention in APP/PS1-dE9 transgenic mice compared with age-matched controls. At clinical and high magnetic field strengths, Gd^{3+}–DOTA–CAT produced greater T_1 relaxivity than Gd^{3+}–DTPA. Tm^{3+}–DOTA–CAT was taken up in a dose-dependent manner in cells over-expressing Cathepsin-D and was shown to transit the blood–brain barrier *in vivo*. This strategy may be useful for the *in vivo* detection of enzyme activity and for the diagnosis of Alzheimer's disease.

Keywords: Cathepsin-D; MRI; fluorescent probe; contrast agent; dual probes; Alzheimer's disease; cellular uptake; cellular imaging

1. INTRODUCTION

Alzheimer's disease (AD) is the most common neurodegenerative disease in adults and afflicts 17 million people worldwide (1). Currently available biomarkers are of limited use for early detection and diagnosis must be made clinically once symptoms are apparent (2,3). However, the pathological changes of AD are believed to begin more than a decade before the development of symptoms, and irreversible damage may already be present at the time of diagnosis (4). Therefore, validated biomarkers to diagnose pre-clinical AD are critically needed.

One potential early marker for AD is Cathepsin-D (Cat-D), a ubiquitously expressed aspartic protease (5,6). Cat-D resides in lysosomes, which are specialized sub-cellular compartments responsible for the degradation of proteins, lipids and carbohydrates. The expansion and accumulation of lysosomes has been reported to be one of the earliest histopathological changes in AD, occurring before the appearance of classical neuropathological changes such as amyloid plaque deposition (7). This expansion is accompanied by upregulation of many lysosomal enzymes, including Cat-D, such that, with advancing disease, Cat-D staining eventually fills neurons (8). Amyloid plaques also contain high levels of biochemically active lysosomal enzymes including Cathepsins B and D (9–11). Cat-D has been shown to be

* *Correspondence to: S. H. Pasternak, J. Allyn Taylor Centre for Cell Biology, Molecular Brain Research Group, Robarts Research Institute, The University of Western Ontario, London, Ontario, Canada. Email: spasternak@robarts.ca*

a *R. Ta, M. Suchy, A. X. Li, T. J. Scholl, R. Bartha*
Imaging Research Group, Robarts Research Institute, The University of Western Ontario, London, Ontario, Canada

b *R. Ta, F. S. Martinez-Santiesteban, T. J. Scholl, R. Bartha*
Department of Medical Biophysics, The University of Western Ontario, London, Ontario, Canada

c *M. Suchy, R. H. E. Hudson*
Department of Chemistry, The University of Western Ontario, London, Ontario, Canada

d *J. H. K. Tam, S. H. Pasternak*
Department of Physiology and Pharmacology, The University of Western Ontario, London, Ontario, Canada

e *J. H. K. Tam, S. H. Pasternak*
J. Allyn Taylor Centre for Cell Biology, Molecular Brain Research Group, Robarts Research Institute, The University of Western Ontario, London, Ontario, Canada

f *S. H. Pasternak*
Department of Clinical Neurological Sciences, The University of Western Ontario, London, Ontario, Canada

upregulated in the cerebrospinal fluid of subjects with AD (12), in subjects with familial AD mutations (13) and in mouse models of AD (14–16). As a result, Cat-D may be an excellent target for the early detection of AD.

Although many other imaging modalities exist, *in vivo* imaging of protease activity by magnetic resonance imaging (MRI) would provide the widest potential clinical benefit owing to the widespread use of MRI scanners. MRI does not expose patients to radiation, and would allow the spatial distribution of detected contrast agent to be automatically registered with the *in vivo* anatomical, functional and chemical information accessible by MRI (17–19).

We have previously reported the synthesis of a dual MRI/fluorescent contrast agent for the detection of Cat-D activity (20) (Fig. 1). This compound consists of an MR imaging moiety that includes a caged lanthanide metal cation, such as Gd^{3+}, to produce T_1-weighted MRI contrast or Tm^{3+} to produce MRI contrast by paramagnetic chemical exchange saturation transfer (PARACEST) (21,22). Oregon Green is also incorporated for optical detection (23). These imaging moieties are conjugated to a peptide backbone containing a Cat-D cleavage site and a Tat sequence derived from the HIV virus that allows penetration through cell membranes and across the blood–brain barrier (BBB) (24). In this strategy, the Tat peptide facilitates transport of the entire molecule across the BBB both into and out of the central nervous system. In the presence of elevated levels of Cat-D, cleavage of the agent at the Cat-D recognition site will release the Tat peptide, trapping the MR visible/Oregon Green components inside the BBB or cell (20). This approach to contrast agent design is similar to the strategy proposed by Roger Tsien's group in conjunction with optical labels and is conceptually similar to the process used in positron emission tomography (PET) imaging that allows fluorodeoxyglucose (FDG) to accumulate in cells as FDG-6-P. One major advantage of this method is that a single Cat-D molecule can cleave multiple contrast agent molecules, leading to accumulation of the contrast agent inside the BBB or cell, with a resulting amplification of the observed signal.

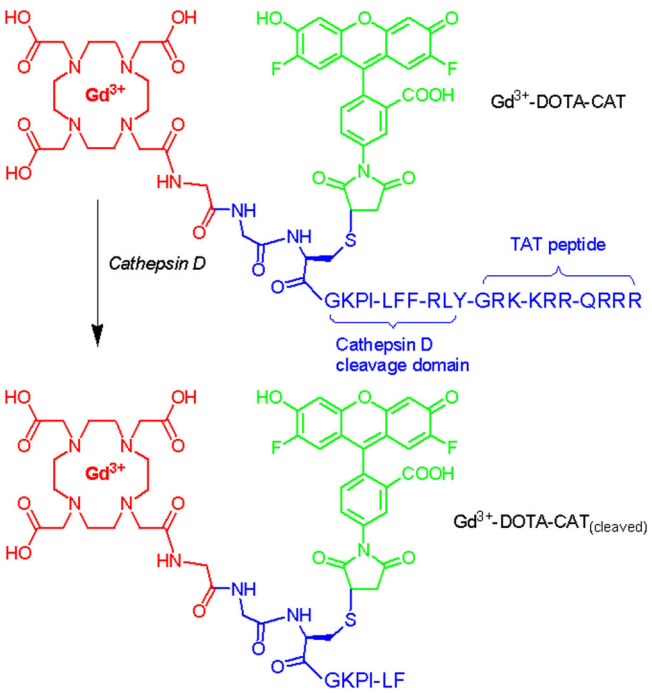

Figure 1. Molecular Structures of Gd^{3+}-DOTA-CAT and Gd^{3+}-DOTA-CAT (cleaved). An imaging moiety consisting of a metal chelator (with Gd^{3+} lanthanide metal cation) for MRI detection (red) and an Oregon Green (green) fluorescent tag for optical detection. These structures are coupled to a peptide backbone consisting of a Cathepsin-D cleavage sequence and a cell-penetrating peptide sequence. In the Tm^{3+}-DOTA-CAT agent, Gd^{3+} is replaced with Tm^{3+}.

We have previously demonstrated that Tm^{3+}–DOTA–CAT is a substrate for Cat-D and is taken up by cells over-expressing Cat-D (20). Although Tm^{3+}–DOTA–CAT can be detected using the on-resonance paramagnetic chemical exchange effect (OPARACHEE) (25), the inclusion of Gd^{3+} in the agent may increase *in vivo* detection sensitivity using T_1-weighted MR imaging. The purpose of the current study was to determine the minimum concentrations required for optical and MR detection, and establish the time course of cellular uptake and retention in the brain in normal mice and a mouse model of Alzheimer's disease.

2. RESULTS

2.1. *In-vitro* MRI: T_1 Relaxivity of Gd^{3+}–DOTA–CAT, Gd^{3+}–DOTA–CAT$_{(cleaved)}$

We examined the relative T_1-weighted signal intensities from tissue phantoms containing a range of concentrations of Gd^{3+}–DOTA–CAT and conventional Gd^{3+}–DTPA in 10% bovine serum albumin at 9.4 T at 37 °C (Fig. 2A). Both agents showed a concentration-dependent increase in T_1-weighted signal intensity with Gd^{3+}–DOTA–CAT generating higher signals than Gd^{3+}–DTPA, indicating more efficient T_1 relaxation with this agent. The T_1 relaxation time constants of each compound at concentrations ranging from 50 to 500 μM were studied. Gd^{3+}–DOTA–CAT had a lower T_1 time constant at each concentration compared with Gd^{3+}–DTPA. To assess the contrast agent's relaxivity within cells, we also evaluated the cleaved form of Gd^{3+}–DOTA–CAT$_{(cleaved)}$. Plotting the relaxation rate ($R_1 = 1/T_1$) as a function of concentration (Fig. 2B), Gd^{3+}–DOTA–CAT had a relaxivity of 6.9 $(mM\,s)^{-1}$ and Gd^{3+}–DOTA–CAT$_{(cleaved)}$ had a relaxivity of 3.3 $(mM\,s)^{-1}$ compared with 3.2 $(mM\,s)^{-1}$ for Gd^{3+}–DTPA at 9.4 T. The R^2 of the slopes were 0.99, 1.0 and 0.99 for Gd^{3+}–DOTA–CAT, Gd^{3+}–DOTA–CAT$_{(cleaved)}$, and Gd^{3+}–DTPA respectively. Therefore, Gd^{3+}–DOTA–CAT and its cleaved form are expected to generate similar signal changes in T_1-weighted MRI as commercially available Gd^{3+}–DTPA at 9.4 T.

2.2. Nuclear Magnetic Relaxation Dispersion Measurements

The relaxivity of contrast agents was measured using a field-cycling relaxometer from 0.01 to 42.5 MHz at 37°C. Figure 2(C) illustrates the nuclear magnetic relaxation dispersion profile, where relaxivity is plotted as a function of magnetic field for the various contrast agents. The overall trend for all samples was a decrease in relaxivity from low to high field strengths until 10 MHz. At physiological temperatures, the relaxivities were lower for all samples compared with relaxivities at room temperature (data not shown).

2.3. Fluorescence Detection of Tm^{3+}–DOTA–CAT and Gd^{3+}–DOTA–CAT

To examine the fluorescence characteristics of the agents, we generated fluorescence intensity curves of Tm^{3+}–DOTA–CAT and Gd^{3+}–DOTA–CAT plotted against their concentrations (Fig. 3).

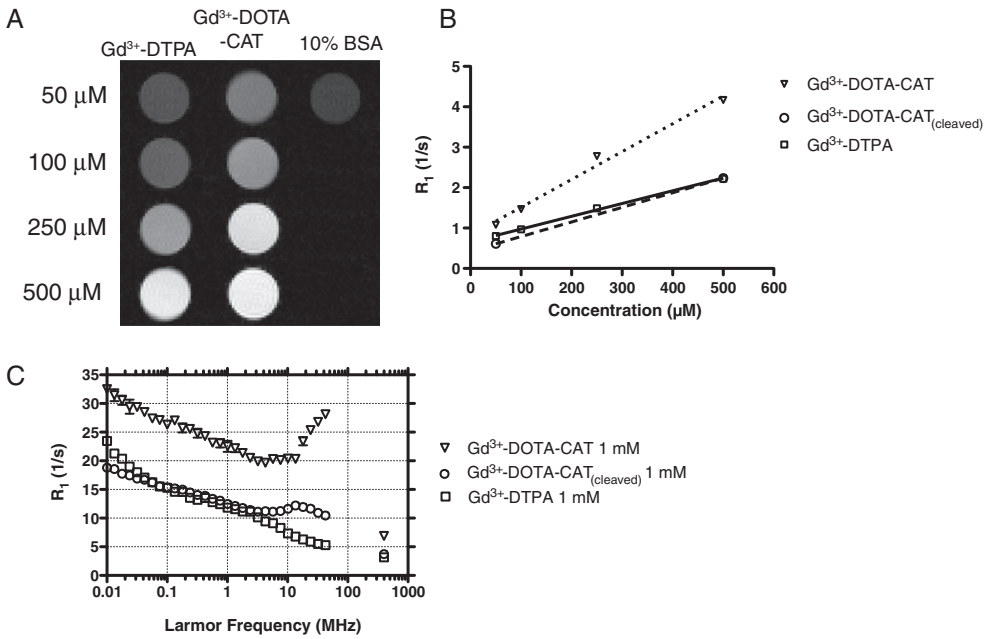

Figure 2. MRI Characterization of Gd^{3+}-DOTA-CAT (A) T_1-weighted images of various concentrations of Gd^{3+}-DTPA and Gd^{3+}-DOTA-CAT in 10% BSA, and 10% BSA alone acquired at 37° C at 9.4T using a spin echo multi-slice pulse sequence with parameters: echo time = 14 ms, repetition time = 50 ms, 2 averages, and 200 μm resolution. (B) Relaxation rate ($R_1 = 1/T_1$) as a function of concentration. Linear best-fitted curves are displayed. Gd^{3+}-DOTA-CAT has a greater relaxivity 6.9 $(mM\ s)^{-1}$ than clinically used Gd^{3+}-DTPA. (C) Proton nuclear magnetic relaxation dispersion curves of 1 mM concentrations of Gd^{3+}-DOTA-CAT (open triangle), Gd^{3+}-DOTA-$CAT_{(cleaved)}$ (open circles), and Gd^{3+}-DTPA (open squares) at 37°C.

Fluorescein isothiocyanate (FITC)–dextran was included as a control. The peak emission for FITC–dextran, Tm^{3+}–DOTA–CAT and Gd^{3+}–DOTA–CAT was 525 nm (data not shown). Both Tm^{3+}–DOTA–CAT and Gd^{3+}–DOTA–CAT were clearly detectable at a concentration of 2 nM and fluorescence increased linearly with concentration. Linear regression curves are shown in Fig. 3 for Tm^{3+}–DOTA–CAT (slope = 0.97, *y*-intercept = 1.7, $R^2 = 0.9995$), Gd^{3+}–DOTA–CAT (slope = 1.09, *y*-intercept = 0.86, $R^2 = 0.9979$), and FITC–dextran (slope = 0.93, *y*-intercept = 3.2, $R^2 = 0.9889$). There was a significant difference between the blank control and each concentration of Tm^{3+}–DOTA–CAT ($p < 0.05$). As expected, FITC–dextran exhibited greater fluorescence intensity than Tm^{3+}–DOTA–CAT and Gd^{3+}–DOTA–CAT, reflecting the higher molar concentration of fluorophore in FITC–dextran.

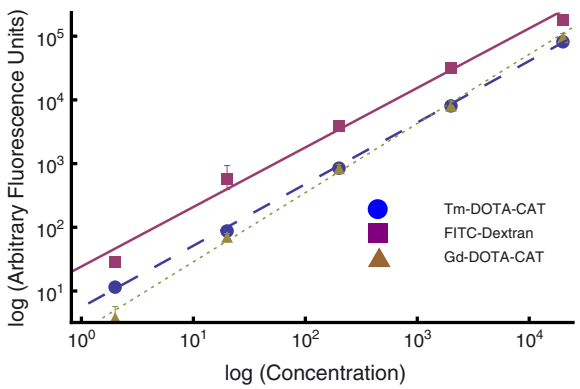

Figure 3. Fluorescent detection of Tm^{3+}-DOTA-CAT and Gd^{3+}-DOTA-CAT. Fluorescence intensity of FITC-Dextran, Tm^{3+}-DOTA-CAT and Gd^{3+}-DOTA-CAT was determined in the concentration range of 2 nM to 20 μM. FITC-Dextran, Tm^{3+}-DOTA-CAT and Gd^{3+}-DOTA-CAT data were fitted to a linear function (regression analysis is provided in the text). All data points were measure in triplicate and displayed as mean ± SD.

2.4. Cellular Uptake of Tm^{3+}–DOTA–CAT

We have previously demonstrated that Tm^{3+}–DOTA–CAT is taken up by SN56 neuronal cells over-expressing Cat-D (20). SN56 cells possess a neuronal morphology and cholinergic phenotype when differentiated (26). Figure 4(A) shows confocal images of the uptake of this agent into cells over-expressing Cat-D–mRFP (Cathepsin-D fused to monomeric Red Fluorescent Protein). SN56 cells were also transfected with the lysosomal membrane protein-1 (LAMP-1)-mRFP as a control for the nonspecific over-expression of a fluorescently tagged lysosomal protein. In these experiments, Cat-D expression led to a clear increase in the number of cells taking up the agent. We quantified agent uptake by counting the number of cells that demonstrated bright green fluorescent signal (Fig. 4B). In these experiments, 72.1 ± 7.7% of Cat-D transfected SN56 cells took up and retained contrast agent in comparison to 7.6 ± 1.1% nontransfected SN56 cells. Of the SN56 cells transfected with LAMP-1, 28 ± 7% of SN56 cells took up and retained contrast agent. One-way ANOVA demonstrated a significant difference between the three groups ($p < 0.0001$). *Post-hoc* Tukey tests were performed between each pair of groups that demonstrated that they are all significantly different ($p < 0.0001$).

We also examined the concentration dependence of agent uptake. Cells were transfected with Cat-D-mRFP and exposed to Tm^{3+}–DOTA–CAT at various concentrations. Uptake was quantified by counting the number of cells bearing bright green fluorescence. In these uptake experiments, 19.0% ± 2.0% of cells exposed to the agent at 5 μM took up Tm^{3+}–DOTA–CAT, and this number increased with concentration so that, at 100 μM, 78.0% ± 6.5% of cells took up the agent. In contrast, a maximum of 4.7% ± 1.3% of cells not over-expressing Cat-D took up the agent over the entire concentration range (Fig. 4C). This difference between nontransfected and transfected SN56 cells is statistically significant at each concentration ($p < 0.05$).

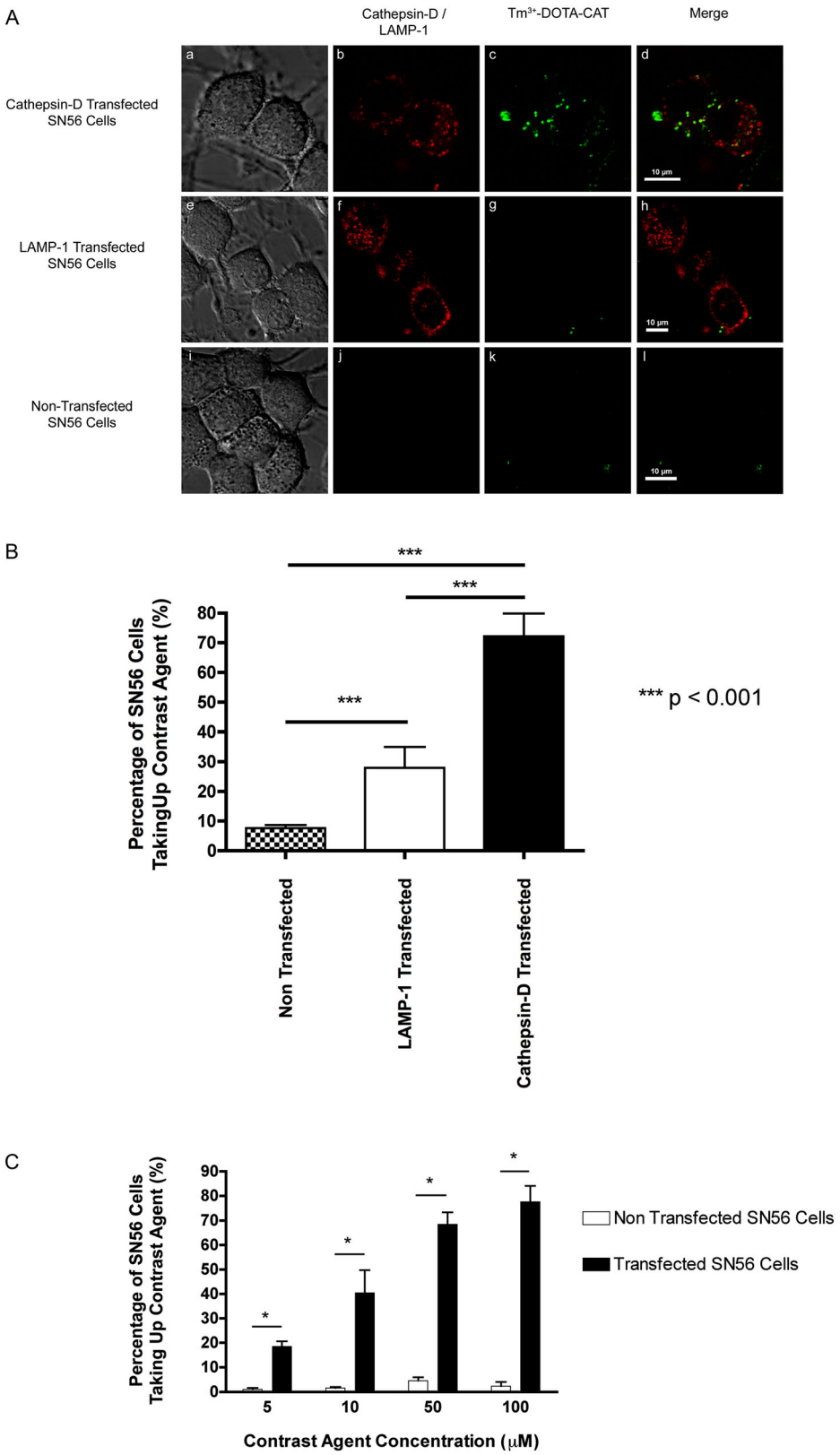

Figure 4. Cat-D expression increases uptake of Tm^{3+}-DOTA-CAT in neuronal SN56 cells. (A) SN56 cells were exposed to 50 µM of Tm^{3+}-DOTA-CAT for 30 minutes. Representative confocal images of Cat-D-mRFP transfected (panels a-d), LAMP-1-mRFP transfected cells (panels e–h), and non-transfected cells (panels i–l). Panels a, e, i are DIC images. b, f, j show Cat-D or LAMP-1 fluorescence (red), Panels C, G, K show Tm^{3+}-DOTA-CAT fluorescence (green). Panels D, H, L are the merged fluorescence channels. (B) Cell counting was performed to analyze the percentage of SN56 cells taking up contrast agent in the three groups. Post-hoc Tukey tests demonstrated a significant difference between all groups ($p < 0.001$). (C) Cellular uptake of Tm^{3+}-DOTA-CAT was observed in a concentration dependent manner in cells over-expressing Cat-D-mRFP. Cell counting was used quantitate the percentage of cells taking up Tm^{3+}-DOTA-CAT after 30 minutes of incubation. The asterisk indicates statistical significance at each time point ($p < 0.05$). Error bars represent standard error of the mean.

2.5. SN56 Neuronal Cell Viability Studies

For a preliminary assessment of the toxicity of this compound, we exposed SN56 cells in culture to 50 μM of Tm^{3+}–DOTA–CAT for varying amounts of time and stained them with trypan blue to identify dead cells. Figure 5 shows that, at 2, 4, 6 and 24 h, 88 ± 4, 88 ± 4, 86 ± 4 and 90 ± 7% of SN56 cells, respectively, were viable. Control cells were left in culture medium for 24 h. There were no significant differences between the percentage of cells surviving in control SN56 cells and SN56 cells exposed to Tm^{3+}–DOTA–CAT up to 24 h.

2.6. Cathepsin-D is Not Increased Overall in APP/PS1-dE9 AD Mice

In order to assess the utility of this reagent, we turned to an Alzheimer's disease mouse model. These mice express the human proteins bearing mutations known to cause familial Alzheimer's disease, namely the amyloid precursor protein (APP) with the Swedish mutation and presenilin-1 with exon 9 deleted (PS1-dE9). APP/PS1-dE9 mice develop age-related cognitive impairment and some of the histological features of AD (amyloid plaques) by 6–9 months of age (27,28). We first examined the expression levels of Cat-D in the brains of 45-day-old and 1-year-old control and APP/PS1-dE9 mice by western blotting (Fig. 6A). In control and APP/PS1-dE9 mice, Cat-D was expressed in an immature (46 kDa) and mature form (33 kDa). Total Cat-D expression was collected from both immature and mature forms of Cat-D expression ($n = 5$). Although 1-year-old mice expressed Cat-D at higher levels than 45-day-old mice, as expected, there was no clear difference between the AD and normal control mice. These blots were then quantified and normalized for protein loading using the structural protein alpha tubulin as a loading control (Fig. 6B). Mean relative density ± SEM was calculated for each of the following groups: 45-day-old controls (0.92 ± 0.02); 45-day-old APP/PS1-dE9 (0.98 ± 0.02); 1-year-old controls (1.28 ± 0.08); and 1-year-old APP/PS1-dE9 (1.40 ± 0.11). There were significant differences between 45-day-old controls and 1-year-old controls ($p < 0.01$) and between 45-day-old APP/PS1-dE9 and 1-year-old APP/PS1-dE9 mice ($p < 0.05$). Although there appeared to be slightly more mature Cat-D in the 1-year-old APP/PS1-dE9 mice than the control mice after normalization, this difference was not statistically significant.

2.7. Cathepsin-D is Elevated in and Around Amyloid Plaques

We were surprised by the similarity between normal and APP/PS1-dE9 mice on western blotting. We hypothesized that differences in Cat-D might be pronounced locally in and around amyloid plaques, as has been demonstrated in human pathological material (9,10). Furthermore, Cat-D in amyloid plaques might be bound up in detergent insoluble material and may not run properly on standard SDS polyacrylamide gels. Alzheimer's disease amyloid plaques are difficult to immunostain using routine techniques and require the antigen to be exposed by pretreatment with formic acid (29). Therefore, we pretreated brain sections with 80% formic acid and stained the sections with antibodies against Aβ42 or Cat-D. These antibodies were then detected using a secondary antibody coupled to the enzyme horseradish peroxidase and reacted with diaminobenzidine, yielding a brown precipitate. Sections were examined by light microscopy at high power (63×). Using these techniques, amyloid plaques were clearly seen with Aβ42 immunostaining in all APP/PS1-dE9 mice examined, as expected (Fig. 7a). Amyloid plaques were observed within the cerebral cortex and the hippocampus (data not shown). When these brain sections were stained with an antibody to Cat-D, staining was also seen in amyloid plaques, where it tended to occur in the outer regions of plaques (Fig. 7b). Cells around the plaques also appear to have a higher level of intracellular Cat-D. In the absence of primary antibody, only the vague outlines of amyloid plaques are visible (Fig. 7c).

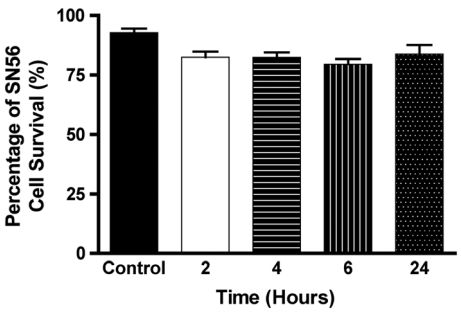

Figure 5. Cell viability of SN56 cells. Cell counting was performed on the light microscopy images of SN56 cells incubated with Tm^{3+}-DOTA-CAT for 2, 4, 6, and 24 hours with trypan blue (n = 3). There were no statistically significant differences in cell survival between any of the time points.

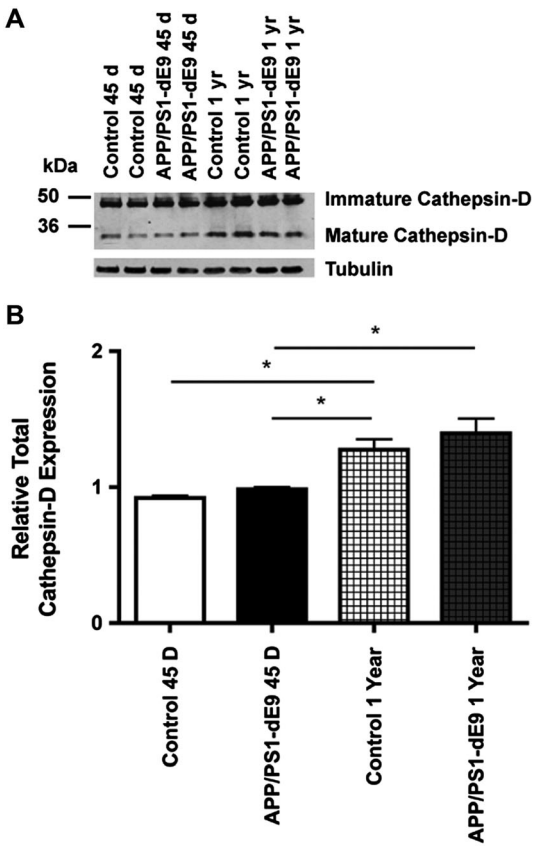

Figure 6. (A) Representative Western blot of the immature and mature forms of Cat-D in 45-day old controls and APP/PS1-dE9 mice and 1-year old controls and APP/PS1-dE9 mice. All lanes were loaded with 20 μg of protein. The blot was re-probed with alpha tubulin as a loading control. (B) Quantification of total Cat-D expression levels. Band intensities were quantified and normalized for loading using alpha tubulin. Data represent mean ± SD from at least 3 individual mice. There were significant differences between the expression of 45-day old controls and 1-year old controls, 45-day old APP/PS1-dE9 and 1-year old APP/PS1-dE9, and between 45-day old APP/PS1-dE9 and 1-year old controls ($p < 0.05$).

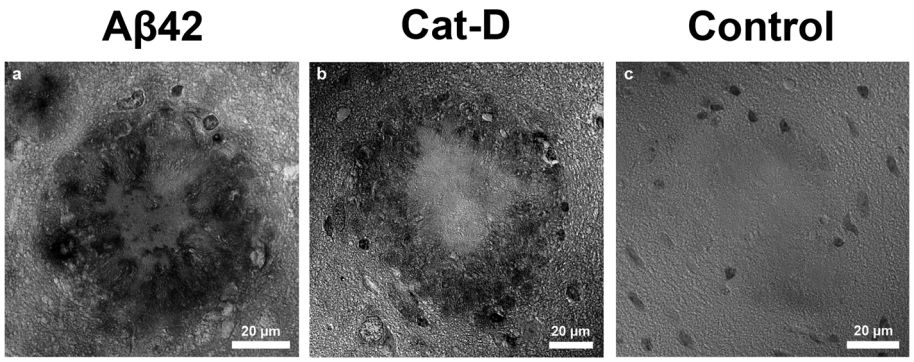

Figure 7. Cat-D is elevated in the extracellular space in amyloid plaques in the cortex of APP/PS1-dE9 mice. Panel a demonstrates the DIC image acquired of Aβ42 DAB staining of an amyloid plaque. Panel b shows Cat-D DAB staining of an amyloid plaque. Panel c is a negative control for DAB stain.

2.8. Contrast Agent Uptake in the Cortical APP/PS1-dE9 and Control Mouse Brain

Figure 8 illustrates Cat-D distribution visualized using confocal microscopy and routine immunofluorescence staining (red) and contrast agent uptake (green) within the cortex immediately dorsal to the hippocampus of both 1-year-old control and 1-year-old APP/PS1-dE9 mice at 30 min post-injection. There was substantial Cat-D staining in a punctate pattern typical of intracellular organelles (lysosomes) in both controls and APP/PS1-dE9 sections illustrating no clear difference between these two groups. Amyloid plaques were not readily apparent. Red blood cells within blood vessels were autofluorescent and appear very bright in both the green and red channels and yellow in the merged image. These images demonstrate that the contrast agent was able to penetrate the blood-brain barrier to transverse into the neuropil as well as into cells containing Cat-D at 30 min post-injection.

To quantify uptake of agent into the neuropil, representative confocal images were acquired from the cortex, dorsal to the hippocampus to cover an area of $101,250\,\mu m^2$. Images were taken in triplicate from two sections in three non-injected ($n=6$), three control ($n=6$) and three APP/PS1-dE9 ($n=6$) mice at each time point (Fig. 9A). The mean pixel intensity of the green channel was determined for each image using ImageJ software and these were averaged for all of the images at each time point (Fig. 9B). Noninjected mice had the lowest mean pixel intensity value 70.0 ± 0.3 (mean $\pm$ SEM) fluorescence units. These noninjected fluorescence values were subtracted from the fluorescence units obtained for control and APP/PS1-dE9 injected mice at each time point. Control mice exhibited substantial green signal at 30 min of 785 ± 88 fluorescence units that declined over time to 220 ± 68 fluorescence units and eventually to 3 ± 3 fluorescence units at 120 min (Fig. 9B). In contrast, APP/PS1-dE9 mice demonstrated increased green signal from 30 min at 295 ± 11 fluorescence units, which rose to 410 ± 69 fluorescence units at 60 min before dropping to 89 ± 14 fluorescence units at 120 min. A two-tailed paired *t*-test was conducted to compare the mean fluorescence levels across images in control-injected, and APP/PS1-dE9 injected mice at each time point. There was a significant difference between the mean fluorescence of control and APP/PS1-dE9 mice at 30 min ($p < 0.05$) and 120 min ($p < 0.05$).

2.9. Contrast Agent Uptake in APP/PS1-dE9 and Control CA1 and CA3 Hippocampus

Since the hippocampus is affected early in human AD, we examined the uptake of contrast agent in the CA1 and CA3 regions of

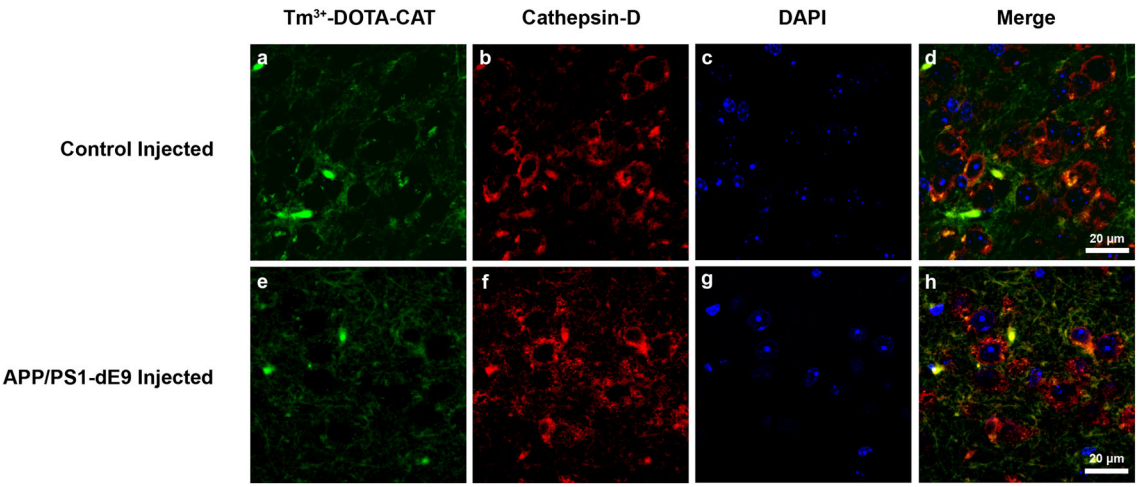

Figure 8. Representative confocal microscopy images of the cerebral cortex in 1-year old control and transgenic APP/PS1-dE9 mice. The first column (a and e) illustrates the amount of fluorescent signal coming from Tm^{3+}-DOTA-CAT (green). The second column (b and f) of images displays the Cat-D staining in red. DAPI nuclear staining is shown in blue (c and g) and the overlay of all channels in the last column (d and h). Red blood cells are seen as discrete autofluorescent rectangles in the red and green channels. The contrast agent produces a diffuse green color throughout the neuropil, which is observed along with Cat-D staining in cells (d and h).

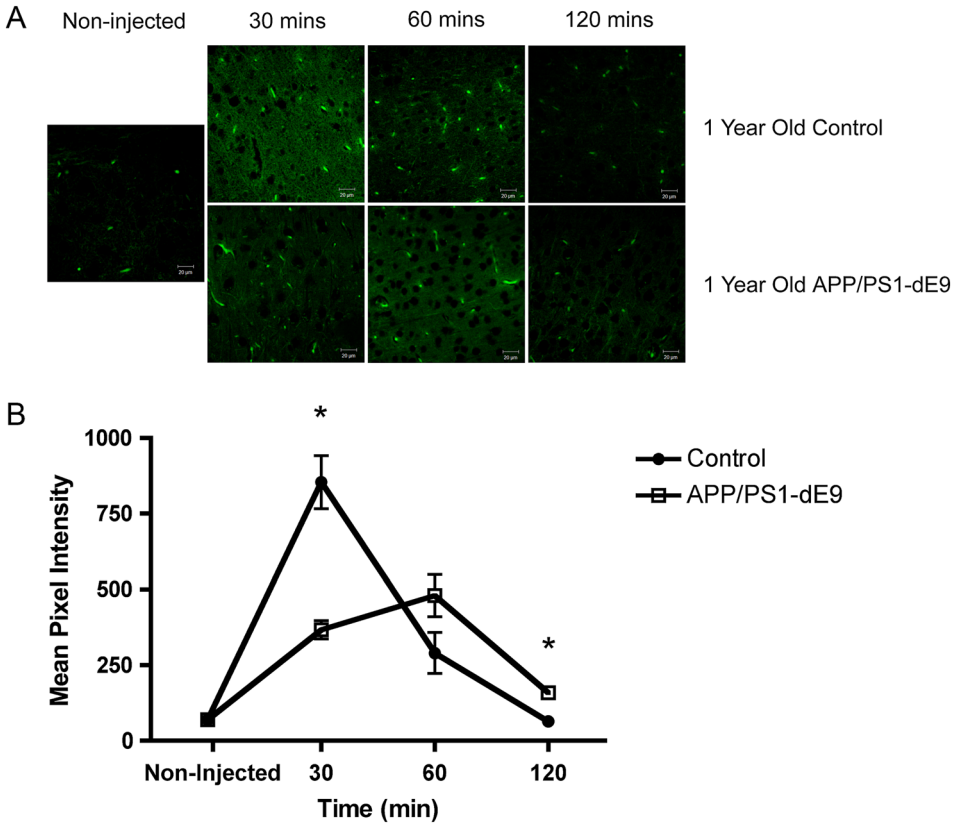

Figure 9. Quantitative uptake of contrast agent in control and APP/PS1-dE9 cortex of the brain. (A) Normal and APP/PS1-dE9 mice received IV injections of contrast agent and were sacrificed at the indicated time point. Coronal sections were taken from each brain and representative images showing contrast agent (green) in cortex directly dorsal to the hippocampus. (B) Mean pixel intensity (± SEM) of the green channel was measured across whole images. Control injected mice exhibited the greatest amount of uptake at 30 minutes and returned to non-injected levels of fluorescence by 120 minutes. APP/PS1-dE9 mice showed a slower uptake of contrast agent, peaking at 60 minutes and demonstrated a greater retention of agent at 120 minutes. The asterisks represent a statistical significance of $p < 0.05$.

the hippocampus of noninjected ($n = 6$), control ($n = 6$) and APP/PS1-dE9 ($n = 6$) injected mice. This analysis was performed using at least three images covering $101,250\,\mu m^2$ from at least two sections performed in triplicate acquired in the CA1 and CA3 regions of control and APP/PS1-dE9 mice at each time point. A two-tailed paired *t*-test was conducted to compare the mean fluorescence levels across images in control-injected, and APP/PS1-dE9 injected mice at each time point. Noninjected mice had a mean fluorescence level of 927 ± 26 fluorescence units (CA 1) and 902 ± 23 fluorescence units (CA 3) (data not shown). These noninjected fluorescence values were subtracted from the fluorescence units obtained for control and APP/PS1-dE9 injected mice at each time point. Figure 10 demonstrates that all injected mice exhibited greater fluorescence levels in the CA1 and CA3 regions than in noninjected mice. In the CA1 region of the hippocampus, control-injected mice had a mean fluorescence level of 197 ± 47 at 30 min, 163 ± 39 at 60 min, and 75 ± 17 fluorescence units at 120 min. APP/PS1-dE9 injected mice had a mean fluorescence level of 68 ± 20 at 30 min, 154 ± 28 at 60 min and 122 ± 26 fluorescence units at 120 min.

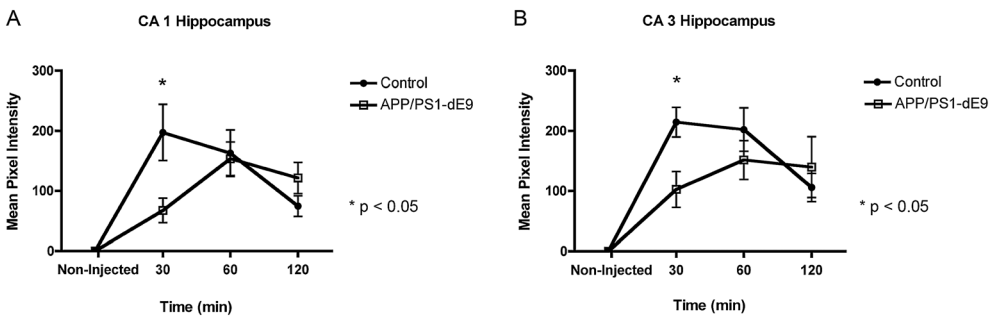

Figure 10. Quantitative uptake of contrast agent in control and APP/PS1-dE9 Hippocampus. CA1 (A) and CA3 (B) hippocampal mean pixel intensities in control and APP/PS1-dE9 after injection of contrast agent. Control injected mice had the greatest amount of uptake at 30 minutes and then exhibited decreasing fluorescence over time in both regions of the hippocampus. APP/PS1-dE9 injected mice exhibited delayed uptake with peak fluorescence levels at 60 minutes with washout occurring at 120 minutes. Similar uptake patterns were observed in both the CA1 and CA3 regions of the hippocampus as compared to that observed in the cortex. The asterisks represent a statistical significance of $p < 0.05$.

The control-injected mice displayed the greatest amount of fluorescence at the 30 min time point and gradually declined over time. In contrast, APP/PS1-dE9 injected mice showed an increasing amount of fluorescence from 30 to 60 min and then an eventual decline at 120 min. Between groups, control-injected mice had greater tissue fluorescence than APP/PS1-dE9 injected mice at 30 min ($p < 0.05$) and a trend towards higher fluorescence at 120 min.

In the CA3 region, both control and in APP/PS1-dE9 injected mice displayed a similar pattern of contrast agent uptake to that observed in the CA1 hippocampus region. Control injected mice had a mean fluorescence level of 215 ± 25 at 30 min, 202 ± 36 at 60 min and 106 ± 23 fluorescence units 120 min. APP/PS1-dE9 injected mice had a mean fluorescence level of 103 ± 30 at 30 min, 152 ± 32 at 60 min and 140 ± 51 fluorescence units at 120 min. Between groups, control-injected mice had greater fluorescence than APP/PS1-dE9 injected mice at 30 min ($p < 0.05$).

2.10. Contrast Agent Uptake in Kidneys and Liver

The mean fluorescence levels were measured in *ex vivo* tissues of the kidneys and liver of injected mice and noninjected control mice (Fig. 11). Noninjected mice had an average fluorescence in the kidney of 0.742 ± 0.061 and in the liver of 0.745 ± 0.367 per mg of tissue. Control injected mice had an average fluorescence in the kidney of 39.3 ± 35.6 and in the liver of 13.8 ± 5.7 per mg of tissue. APP/PS1-dE9 injected mice had an average fluorescence in the kidney of 19 ± 11.6 and in the liver of 7.2 ± 5.4. In kidney samples, there was a significant difference between the average fluorescence values in noninjected mice and APP/PS1-dE9 injected mice ($p < 0.05$). In liver samples, there was a significant difference between the average fluorescence values in noninjected mice and control-injected mice ($p < 0.01$).

Noninjected kidney and liver fluorescence values were then subtracted from all other values. The concentration of agent within the tissue was estimated by comparing the remaining tissue signal to the fluorescence calibration curve in Fig. 3. Control injected kidney contained 7.8 nM of Tm^{3+}–DOTA–CAT, control injected liver: 2.0 nM of Tm^{3+}–DOTA–CAT, APP/PS1-dE9 injected kidney contained 3.2 nM of Tm^{3+}–DOTA–CAT, and APP/PS1-dE9 injected liver contained 0.6 nM of Tm^{3+}–DOTA–CAT at 30 min post-injection.

3. DISCUSSION

In the current study, a strategy is presented to diagnose Alzheimer's disease that may be useful at the earliest stages of the disease. This strategy is based on the observation that the upregulation of lysosomes and lysosome-related organelles and enzymes are a very early event in AD. The goal of this study was to demonstrate the tissue uptake and retention of a novel type of MRI/fluorescent contrast agent targeting the activity of the lysosomal enzyme Cat-D. The agent incorporates a caged lanthanide metal ion coupled to a Tat peptide via a Cat-D cleavage site. The Tat peptide allows the agent to cross the blood brain barrier and cell membranes in both directions. In a compartment enriched in Cat-D, cleavage of the agent released the Tat peptide, slowing the exit of the agent from that compartment. Here we present two variations of the contrast agent and demonstrate that these agents can be detected experimentally using both MRI and optical imaging techniques.

Specifically, we demonstrated detection of Gd^{3+}–DOTA–CAT by MRI in a concentration range from 50 to 500 μM, where it exhibited greater sensitivity than clinically used Gd^{3+}–DTPA at 9.4 T. *In vitro* MRI data has been supplemented with relaxation rate measurements of Gd^{3+}–DOTA–CAT and Gd^{3+}–DOTA–CAT$_{(cleaved)}$ at magnetic field strengths ranging from 0.24 mT to 9.4 T. The experimentally observed relaxivity for Gd^{3+}–DTPA was also verified in similar *in vitro* studies (30,31). Previously, Tm^{3+}–DOTA–CAT was also detected by MRI using OPARACHEE contrast at 0.5–4 mM concentrations at 9.4 T (20). The relaxivity of Gd^{3+}–DOTA–CAT was slightly higher than the cleaved form of the Gd compound, which had a relaxivity that was comparable to other reported Gd^{3+}–DOTA–monoamide complexes. The Gd^{3+}–DOTA–CAT$_{(cleaved)}$ compound has a slightly greater relaxivity at lower field strengths than Gd^{3+}–DOTA–Arg_8, as reported by Endres *et al.* (32). However, Gd^{3+}–DOTA–CAT$_{(cleaved)}$ has a similar relaxivity to Gd^{3+}–DOTA–Arg_8 at higher field strengths where the relaxivity differences begin to diminish as expected.

The relaxivities of Gd^{3+}–DTPA, Gd^{3+}–DOTA–CAT, and Gd^{3+}–DOTA–CAT$_{(cleaved)}$, in 10% heat-treated BSA at pH 7 were measured at fields ranging from 0.24 mT to 9.4 T. Generally, relaxivity decreased as a function of field strengths similar to previous results (33). The NMRD profiles were similar to that shown for heat-treated BSA tissue phantoms and human brain tissues

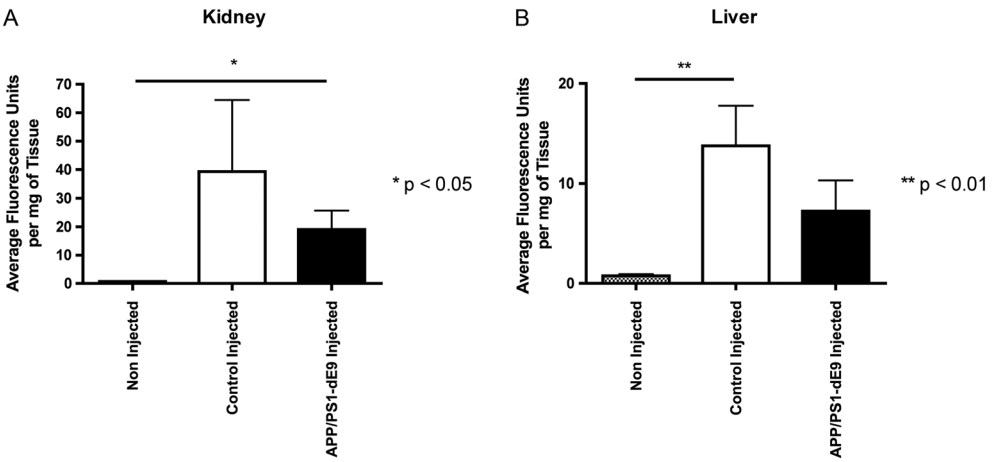

Figure 11. Tm^{3+}-DOTA-CAT uptake in kidney and liver tissues in non-injected, control injected, and APP/PS1-dE9 injected mice. Ex-vivo tissues were obtained 30 minutes post-injection and weighed to provide average fluorescence units per mg of tissue. (A) There was a significant difference between the average fluorescence units between non-injected and APP/PS1-dE9 injected mice ($p < 0.05$) in the kidneys. In the liver (B), there was a significant difference between the average fluorescence units between non injected and control injected mice ($p < 0.01$). Error bars represent standard error of the mean.

(34). In contrast there is little change in relaxivity from 0.01 to 1 MHz in aqueous solutions of BSA (35). Relaxivities decreased at physiological temperatures compared with room temperatures consistent with the pattern observed for similar Gd-based compounds (35). Several studies have observed that relaxivities may change following internalization of a contrast agent within liposomes (36), endosomes or cellular organelles (37), although this property was not evaluated in the study.

In the current work, the relaxivity of the agent was studied in BSA to model the magnetization transfer effect that would be expected in the extracellular environment as well as the intracellular matrix. However, future studies will evaluate the effects of restricted diffusion or altered pH within encapsulated cellular compartments.

For maximum sensitivity, the contrast agent developed in the current study should be sensitive to Cat-D in both the extracellular and intracellular environment. Although an extracellular target is preferred to avoid complications related to absorption and excretion of the agent, the earliest cellular changes in Alzheimer's disease occur in the intracellular compartment. Therefore an agent sensitive to such intracellular changes would provide the earliest warning of pathological damage.

In the current study, Tm^{3+}–DOTA–CAT was taken up and retained by SN56 neuronal cells over-expressing Cat-D in a concentration-dependent manner with minimal toxicity. Images of the agent in these cells suggest that it is taken up into intracellular compartments (likely the endosomal/lysosomal system) rather than in the cytoplasm. The contents of these compartments are in constant flux and therefore the compound and its lanthanide metal will likely be easily excreted from the cell eventually, making it less likely to cause toxicity. This effect was observed during the *in vivo* injection experiment, where the vast majority of the agent left the brain within 2 h. Although contrast agents containing paramagnetic lanthanide metals are generally considered safe (35), future safety studies will be performed to evaluate the safety profile of the agent in the intracellular environment. Currently, it cannot be unambiguously stated that the observed differences in retention of the contrast agent in normal and AD mice is owing to the specific ability of the contrast agent to cross the BBB and be trapped in the brain. We are currently in the process of synthesizing several alternative versions of the compound including versions containing an uncleavable spacer and scrambled Cat-D recognition site to further validate the specificity of the agent and to study its behavior in intracellular compartments.

Although we were initially surprised that the APP/PS1-dE9 mice did not express significantly elevated levels of Cat-D overall compared with control mice, these mice did clearly express Cat-D at higher levels in cells around amyloid plaques and in the plaques themselves, that is, in the extracellular space. This enzyme bound up in amyloid plaques was possibly very difficult to extract and likely underestimated on western blotting experiments. This agrees with studies performed by Cataldo *et al.* (9,10), demonstrating that Cat-D was found extracellularly within amyloid plaques. Despite having similar levels of Cat-D on western blotting overall, the agent had clearly different uptake and retention kinetics in Alzheimer's disease and control mice. Therefore, the Cat-D in and around amyloid plaques may be responsible for the significant difference in uptake and retention of contrast agent. Because the Tat peptide is required for crossing the blood-brain barrier, it is possible that extracellular Cat-D is responsible for 'trapping' in the brain, and not intracellular Cat-D. Note that Cathepsin-E (Cat-E) can also cleave our agent at the same recognition site as Cat-D. Since Cat-E is also elevated in plaques in AD (38), sensitivity to both Cat-D and Cat-E could provide increased detection sensitivity within the context of AD.

The contrast agent was detected fluorescently in the kidneys and liver. At 30 min post-injection the agent appeared in the kidneys of both control and APP/PS1-dE9 injected mice. Future studies would be aimed at evaluating the uptake of agent in the kidneys and liver for up to 24, 48 and 72 h post-injection. Although we have utilized the fluorescent tag as an estimate of contrast agent concentration, it would be useful to incorporate other methods of verifying contrast agent concentration in cells and tissues, that is, through gadolinium quantification using ICP/MS as performed by Aime *et al.* (39).

Currently, the leading candidates in probes for diagnostic imaging in AD are amyloid binding compounds such as the Pittsburgh B (40) compound and florbetapir (41). These compounds bind to β-amyloid aggregates in the brain and are detected using PET. Whether Pittsburgh B or florbetapir-PET imaging constitute good biomarkers for AD also depends on whether β-amyloid burden in plaques in the brain is indeed the earliest or best pathology on which to focus. The diagnostic use of these agents is limited by substantial overlap in signals between controls, subjects with mild AD/mild cognitive impairment, and AD (42–45). In other words some AD patients do not take up these compounds, and many normal controls have high uptake. Sorting out the importance of these findings will require extended follow up of affected individuals. In addition, there is significant evidence that the insoluble fibrillar amyloid in plaques that amyloid agents bind might not be the most relevant form of amyloid. In fact the earliest cognitive changes correlate with soluble diffusible amyloid species (46–48). By focusing on changes in lysosomal biochemistry, it is possible that we may be able to identify metabolically abnormal cells and tissues before there is substantial amyloid accumulation or neurodegeneration.

4. CONCLUSIONS

In this study, we evaluate the MR and fluorescent detection properties and present our first animal data in the development of an MRI/fluorescent contrast agent to quantify enzymatic activity and its potential application to Alzheimer's disease. Despite our selection of an AD mouse model that does not have a large change in total Cat-D expression from controls at one year of age, these animals had increased Cat-D expression in and around amyloid plaques, and our data demonstrates a distinct difference in the uptake and retention of Tm^{3+}–DOTA–CAT over a 2 h period post-contrast injection. A preliminary study of kidney and liver uptake of contrast agent was also presented. Future studies will extend our understanding of the uptake and retention characteristics of this agent across different AD mouse strains and across the lifespan of the animals, with the goal being to identify the earliest time point in which we can distinguish controls from AD. Therefore this agent shows significant potential as a molecular imaging probe for AD.

5. EXPERIMENTAL

5.1. Synthesis and Characterization of Gd^{3+} and Tm^{3+}–DOTA–CAT

Tm^{3+}–DOTA–CAT was synthesized and characterized by high-resolution electron spray ionization mass spectrometry (HR-ESI-MS)

as described in Suchy *et al.* (20). Gd^{3+}–DOTA–CAT and Gd^{3+}–DOTA–$CAT_{(cleaved)}$ were prepared similarly (20), using $GdCl_3 \cdot 6H_2O$; the molecules were characterized by HR-ESI-MS as follows: Gd^{3+}–DOTA–CAT, HRMS (ESI) *m/z*, found 3852.8175 $[M-2H]^+$ (3852.8009 calculated for $C_{166}H_{249}F_2GdN_{53}O_{40}S$); Gd^{3+}–DOTA–$CAT_{(cleaved)}$, HRMS (ESI) *m/z*, found 1894.6071 $[M-2H]^+$ (1894.6072 calculated for $C_{81}H_{101}F_2GdN_{15}O_{24}S$).

5.2. Magnetic Resonance Imaging

To study the T_1 effect of agent concentration on image contrast, a series of 10% (w/v) heat-treated (samples heated in an 80 °C water bath for 10 min) bovine serum albumin (BSA; Sigma Aldrich, St Louis, MO, USA) tissue phantoms containing a range of Gd^{3+}–DOTA–CAT and Gd^{3+}–DOTA–$CAT_{(cleaved)}$ concentrations (0–500 μM) were prepared as in Ropele *et al.* (49). These agents were compared with the standard and widely used contrast agent Gd^{3+}–DTPA (Bayer Healthcare Pharmaceuticals Inc., Germany) in 10% BSA as above. T_1-weighted images of the Gd^{3+}–DOTA–CAT and Gd^{3+}–DTPA phantoms were acquired on a 9.4 T small animal MRI scanner (Agilent, Palo Alto, CA, USA) using a spin-echo multi-slice pulse sequence [field of view, 25.6 × 25.6 mm^2; data matrix, 128 × 128; repetition time (*TR*), 50 ms; echo time (*TE*), 14 ms; two averages; and 5 mm thickness] at 37 °C. The T_1 time constants were measured using an inversion prepared spin-echo multi slice pulse sequence [*TE*, 14 ms; *TR*, 50 ms; inversion time (*TI*), 0, 10, 20, 40, 80, 160, 320, 640, 1280 and 2500 ms; two averages]. The T_1 time constant of each solution was measured by fitting a single exponential curve to the signal intensity as a function of the inversion times. The inverse of the longitudinal relaxation time ($R_1 = 1/T_1$) was plotted against concentration and fit to a straight line to estimate the relaxivity.

5.3. Nuclear Magnetic Relaxation Dispersion Measurements

^{1}H nuclear magnetic relaxation dispersion (NMRD) measurements of 1 mM Gd^{3+}–DTPA, Gd^{3+}–DOTA–CAT, and Gd^{3+}–DOTA–$CAT_{(cleaved)}$, in 10% heat-treated BSA at pH 7 were performed on a fast field-cycling relaxometer (Spinmaster FFC-2000 1 T C/DC, Stelar s.r. l., Mede, Italy). Samples of 400 μL of the contrast agent were prepared in 5-mm NMR tubes (Norell, NJ, USA) and temperature controlled to either 25 or 37 °C using heated air during measurement. The T_1-dispersion curves were measured over 30 points logarithmically distributed over the frequency range 0.01–42.5 MHz (0.24 mT to 1.0 T). The T_1 at each relaxation field was determined by an exponential fit of the signal intensity as a function of 16 relaxation field durations, measured at a readout field of 0.38 T using fast field-cycling between field strengths. R_1-values ($1/T_1$) were obtained with a typical error of less than 2%. NMRD profiles presenting measurement of proton relaxation rates as a function of applied magnetic field are shown in Fig. 2(C).

5.4. Detection Limit of Tm^{3+}–DOTA–CAT and Gd^{3+}–DOTA–CAT by Fluorescence

To determine the emission peak, emission spectra were obtained at 5 nm intervals for samples of 50 μM FITC–dextran (Sigma Aldrich, St Louis, MO, USA), 1 mM Tm^{3+}–DOTA–CAT, and 1 mM Gd^{3+}–DOTA–CAT excited at 488 nm. Serial dilutions of both compounds were performed to create a range of concentrations (1 nM to 10 μM). All samples were prepared in a 96-well black plate (Corning Costar, Lowell, MA, USA) in triplicate ($n = 3$), sampled by SpectraMax5 (Molecular Devices, Sunnyvale, CA, USA) and analyzed by SoftMax Pro data analysis software (Molecular Devices, Sunnyvale, CA, USA).

5.5. Cell Culture

SN56 cells were a gift from Dr Jane Rylett (The University of Western Ontario). SN56 cells were derived from septum neurons (Septal neurons X neuroblastoma N18TG2) (50) and present a number of neuronal features including expression of synaptic vesicle proteins (51) and neuronal type calcium channels. These features are increased by differentiation (52,53). Cells were maintained in Dulbecco's modified Eagle's medium (Gibco) supplemented with 5% fetal bovine serum (HyClone) and 1% penicillin–streptomycin (Gibco). Cell differentiation was performed with the addition of 1 mM dibutyryl-cyclic AMP in the same medium without fetal bovine serum for 24 h. Transient transfections were performed with plasmid expressing a Cat-D–mRFP ($n = 3$) or LAMP-1–mRFP ($n = 5$) using Lipofectamine 2000 Reagent (Invitrogen) according to manufacturer's instructions as previously described (54). Nontransfected cells ($n = 5$) were treated with Lipofectamine 2000 only as a control prior to contrast agent uptake.

5.6. Cellular Uptake and Confocal Microscopy

SN56 cells were grown in 35 mm glass-bottomed culture dishes (MatTek Corporation, Ashland, MA, USA). SN56 cells were incubated at 37 °C for 30 min with 50 μM Tm^{3+}–DOTA–CAT added to cell culture media. Cells were washed three times with Hanks buffered saline solution (Invitrogen) and imaged using a Zeiss LSM 510-Meta laser-scanning confocal microscope (Carl Zeiss, Germany) using a 63× 1.4 numerical aperture oil immersion lens. The contrast agent was visualized using a 488 nm excitation laser and a 500–530 nm emission band pass filter set. Red fluorescence from the Cat-D–mRFP ($n = 3$) or LAMP-1–mRFP ($n = 5$) was imaged using a 543 nm excitation laser and long pass 560 nm filter set. Uptake was quantified by counting the number of cells that had taken up green fluorescent Tm^{3+}–DOTA–CAT by an observer blinded to their Cat-D expression. Nontransfected SN56 cells ($n = 5$) were also counted to quantify nonspecific contrast agent uptake.

5.7. Cell Viability Studies

SN56 cells were seeded in 12-well plates and incubated overnight before treatment of 50 μM Tm^{3+}–DOTA–CAT. Following the indicated incubation time (0, 2, 4, 6 and 24 h), cell density and viability were determined by 0.4% trypan blue exclusion in triplicate. Light microscope images were acquired (10× lens) in five random areas within a well and cell counting was performed to quantify cell death.

5.8. Mice

All animal studies were conducted in accordance with the guidelines of the Subcommittee on Animal Care at the University of Western Ontario, and conformed to the Canadian Council on Animal Care guide for the care and use of laboratory animals. One-year-old APP-Swedish/PS1-dE9 transgenic Alzheimer's disease mice (Jackson Laboratories, Bar Harbor, ME, USA) and age-matched controls BL/6 (Jackson Laboratories, Bar Harbor, ME, USA) were gifts from Drs Marco A.M. Prado and Vania Prado (The University of Western Ontario). These double transgenic

mice express a chimeric mouse/human amyloid precursor protein bearing a Swedish mutation (Mo/HuAPP695swe) and a mutant human presenilin-1 with a deletion in exon 9 (PS1-dE9) and develop amyloid plaques after the age of 6 months (27). In the current study, a total of eight control animals and nine APP/PS1-dE9 mice were studied. Three mice were studied at each time point (30, 60 and 120 min), except for control mice at 30 min ($n = 2$).

5.9. Western Blotting and Antibodies

All cell and tissue lysates were prepared using protease cocktail inhibitors (Roche, Mississauga, Ontario, Canada) with pepstatin A from the cerebral cortex of APP/PS1-dE9 and age-matched control mice. Lanes were run with 20 μg of protein on a 12% SDS–polyacrylamide gel and the resolved proteins were transferred to a nitrocellulose membrane (Bio-Rad, Mississauga, Ontario, Canada) using a Trans-Blot® Semi-Dry Electrophoretic Transfer Cell (Bio-Rad, Mississauga, Ontario, Canada). The membrane was blocked with 5% nonfat milk (w/v) dissolved in Tris buffered saline 0.05% Tween-20. Blots were probed using Anti-Cat-D antibody (Santa Cruz Biotechnology, Santa Cruz, CA, USA), and detected using rabbit-anti-goat coupled to horseradish peroxidase using enhanced chemiluminescence and exposed to CL-Xposure film (Thermo Scientific). Blots were re-probed with anti-Alpha-tubulin (Sigma Aldrich, St Louis, MO, USA) as a loading control. Since immature Cat-D is also the active form and performs the same enzymatic functions as the mature form, both forms were grouped into a total Cat-D expression (5). Films were scanned and quantified using ImageJ (http://rsbweb.nih.gov/ij/).

5.10. Cathepsin-D in Extracellular Amyloid Plaques

Mouse brains were paraffin embedded and sectioned into 5 μM thick coronal sections. To detect amyloid plaques, sections were treated with 80% formic acid for 5 min then stained with antibodies against Aβ42 (custom-made). To detect Cat-D, sections were stained with antibodies against Cat-D (Santa Cruz Biotechnologies, Santa Cruz, CA, USA). The primary antibody was detected with a secondary antibody conjugated to horseradish peroxidase and developed with a diaminobenzidine stain using Vectastain ABC kit (Vectorlabs, Burlington, Ontario, Canada). Sections were imaged on a Zeiss LSM 510 META laser-scanning confocal microscope (Carl Zeiss, Germany) using a 63 × 1.4 numerical aperture oil immersion lens.

5.11. Contrast Agent Uptake in APP/PS1-dE9 and Control Mouse Brain Tissues

Mice were anesthetized with 4% isofluorane and oxygen (1 l min^{-1}). A tail-vein catheter was established and a saline flush was performed to ensure the catheter was accurately placed. Mice were injected intravenously with 100 μl of 1 mM Tm^{3+}–DOTA–CAT over four min using a Harvard Apparatus PHD 2000 programmable pump (Instech Laboratories, Plymouth Meeting, PA, USA). Post-injection, mice were sacrificed at 30 min ($n = 3$ for APP/PS1-dE9; $n = 2$ for controls), 60 min ($n = 3$ for APP/PS1-dE9; $n = 3$ for controls), 120 min ($n = 3$ for APP/PS1-dE9; $n = 3$ for controls) and the brain was extracted. The prefrontal cortex was removed, placed on dry ice and stored at −80 °C for western blotting. The rest of the brain was fixed in 10% neutral buffered formalin for at least 48 h.

5.12. Histological Analysis of Transgenic APP/PS1-dE9 and Control mice

Mouse brains were paraffin embedded and sectioned into 5 μM thick coronal sections. To detect Cat-D, sections were processed using a 2100 Retriever (Pick Cell Laboratories, Lelystad, Netherlands) and stained with antibodies against Cat-D (Santa Cruz Biotechnology, Santa Cruz, CA, USA). Antibodies were detected using an AlexaFluor 543 (red) anti-rabbit secondary for immunofluorescence (Molecular Probes) and nuclei were counterstained with DAPI (4′,6-Diamidino-2-Phenylindole, Dihydrochloride; Sigma-Aldrich, St Louis, MO, USA). Sections were imaged by confocal microscopy on a Zeiss LSM 510 META laser-scanning confocal microscope (Carl Zeiss, Germany) using a 63× 1.4 numerical aperture oil immersion lens. The contrast agent was visualized using a 488 nm excitation laser and a 500–530 nm emission band pass filter set. Red fluorescence from Cat-D immunostain was imaged using a 543 nm excitation laser and long pass 560 nm filter set. Blue fluorescence from DAPI staining was imaged using a two-photon Chameleon excitation laser at 750 nm and 390-465 nm emission band pass filter set. Mean pixel intensity was analyzed across the image for each time point using ImageJ (http://rsbweb.nih.gov/ij/). Mean pixel intensity levels were assigned to each group and their respective time points expressed as mean ± SEM. Each set of images were acquired on the same day and with identical acquisition settings.

To examine the uptake within the cortex, CA1, and CA3 regions of the hippocampus, noninjected mean pixel intensity values were subtracted from control-injected and APP/PS1-dE9 injected mean pixel intensity values. Two-tailed paired *t*-tests were performed using Prism5, (GraphPad, La Jolla, CA, USA) to compare the mean pixel intensity in images between control-injected and APP/PS1-dE9 injected mice at each time point.

5.13. Liver and Kidney Contrast Agent Uptake

Liver and kidneys were extracted from control injected ($n = 2$) and APP/PS1-dE9 injected ($n = 3$) mice 30 min post-injection. Noninjected ($n = 4$) control BL/6 mice (Jackson Laboratories, MA, USA) were used as a negative control for the liver and kidneys. Tissue samples were weighed and then homogenized in protein extraction buffer (with protease inhibitors Roche and pepstatin A). Samples were then centrifuged at 8000 rpm for 15 min at 4 °C. The supernatant from each sample was removed and placed in a 96 black-well plate (Costar, Lowell, MA, USA). A fluorescence plate reader (Molecular Devices, Sunnyvale, CA, USA) was used to measure the relative fluorescence levels of each sample compared with noninjected controls. Excitation of the Oregon green portion of the contrast agent was at 488 nm with an emission wavelength of 525 nm. Fluorescence values are reported as average fluorescence per milligram of tissue. Statistical analysis was performed using two-tailed *t*-tests to compare the groups.

Acknowledgments

The authors gratefully acknowledge funding received from the National Science and Engineering Research Council of Canada, Operating Grant MOP 104148 from the Canadian Institute of Health Research, and the Ontario Institute for Cancer Research to support this work. Gifts of materials are gratefully acknowledged from Professors Roger Tsein (University of California, San Diego), Jane Rylett (The University of Western Ontario), and Marco Prado and Vania Prado (The University of Western Ontario).

REFERENCES

1. Ferri CP, Prince M, Brayne C, Brodaty H, Fratiglioni L, Ganguli M, Hall K, Hasegawa K, Hendrie H, Huang Y, Jorm A, Mathers C, Menezes PR, Rimmer E, Scazufca M. Global prevalence of dementia: a Delphi consensus study. Lancet 2005; 366(9503): 2112–2117.
2. Cummings JL. Alzheimer's disease. New Engl J Med 2004; 351(1): 56–67.
3. Feldman HH, Jacova C, Robillard A, Garcia A, Chow T, Borrie M, Schipper HM, Blair M, Kertesz A, Chertkow H. Diagnosis and treatment of dementia: 2. Diagnosis. CMAJ 2008; 178(7): 825–836.
4. Golde TE, Petrucelli L, Lewis J. Targeting Abeta and tau in Alzheimer's disease, an early interim report. Exp Neurol 2010; 223(2): 252–266.
5. Benes P, Vetvicka V, Fusek M. Cathepsin D – many functions of one aspartic protease. Crit Rev Oncol Hematol 2008; 68(1): 12–28.
6. Zaidi N, Maurer A, Nieke S, Kalbacher H. Cathepsin D: a cellular roadmap. Biochem Biophys Res Commun 2008; 376(1): 5–9.
7. Cataldo AM, Hamilton DJ, Nixon RA. Lysosomal abnormalities in degenerating neurons link neuronal compromise to senile plaque development in Alzheimer disease. Brain Res 1994; 640(1–2): 68–80.
8. Cataldo AM, Hamilton DJ, Barnett JL, Paskevich PA, Nixon RA. Properties of the endosomal–lysosomal system in the human central nervous system: disturbances mark most neurons in populations at risk to degenerate in Alzheimer's disease. J Neurosci 1996; 16(1): 186–199.
9. Cataldo AM, Nixon RA. Enzymatically active lysosomal proteases are associated with amyloid deposits in Alzheimer brain. Proc Natl Acad Sci USA 1990; 87(10): 3861–3865.
10. Cataldo AM, Paskevich PA, Kominami E, Nixon RA. Lysosomal hydrolases of different classes are abnormally distributed in brains of patients with Alzheimer disease. Proc Natl Acad Sci USA 1991; 88(24): 10998–11002.
11. Nixon RA, Cataldo AM, Mathews PM. The endosomal–lysosomal system of neurons in Alzheimer's disease pathogenesis: a review. Neurochem Res 2000; 25(9–10): 1161–1172.
12. Schwagerl AL, Mohan PS, Cataldo AM, Vonsattel JP, Kowall NW, Nixon RA. Elevated levels of the endosomal–lysosomal proteinase cathepsin D in cerebrospinal fluid in Alzheimer disease. J Neurochem 1995; 64(1): 443–446.
13. Bagnoli S, Nacmias B, Tedde A, Guarnieri BM, Cellini E, Ciantelli M, Petruzzi C, Bartoli A, Ortenzi L, Serio A, Sorbi S. Cathepsin D polymorphism in Italian sporadic and familial Alzheimer's disease. Neurosci Lett 2002; 328(3): 273–276.
14. Cataldo AM, Peterhoff CM, Schmidt SD, Terio NB, Duff K, Beard M, Mathews PM, Nixon RA. Presenilin mutations in familial Alzheimer disease and transgenic mouse models accelerate neuronal lysosomal pathology. J Neuropathol Exp Neurol 2004; 63(8): 821–830.
15. Howlett DR, Bowler K, Soden PE, Riddell D, Davis JB, Richardson JC, Burbidge SA, Gonzalez MI, Irving EA, Lawman A, Miglio G, Dawson EL, Howlett ER, Hussain I. Abeta deposition and related pathology in an APP × PS1 transgenic mouse model of Alzheimer's disease. Histol Histopathol 2008; 23(1): 67–76.
16. Wirths O, Breyhan H, Marcello A, Cotel MC, Bruck W, Bayer TA. Inflammatory changes are tightly associated with neurodegeneration in the brain and spinal cord of the APP/PS1KI mouse model of Alzheimer's disease. Neurobiol Aging 2010; 31(5): 747–757.
17. Rosen Y, Lenkinski RE. Recent advances in magnetic resonance neurospectroscopy. Neurotherapeutics 2007; 4(3): 330–345.
18. Vemuri P, Jack CR, Jr. Role of structural MRI in Alzheimer's disease. Alzheimers Res Ther 2010; 2(4): 23.
19. Sperling RA, Dickerson BC, Pihlajamaki M, Vannini P, LaViolette PS, Vitolo OV, Hedden T, Becker JA, Rentz DM, Selkoe DJ, Johnson KA. Functional alterations in memory networks in early Alzheimer's disease. Neuromolecular Med 2010; 12(1): 27–43.
20. Suchy M, Ta R, Li AX, Wojciechowski F, Pasternak SH, Bartha R, Hudson RH. A paramagnetic chemical exchange-based MRI probe metabolized by cathepsin D: design, synthesis and cellular uptake studies. Org Biomol Chem 2010; 8(11): 2560–2566.
21. Viswanathan S, Kovacs Z, Green KN, Ratnakar SJ, Sherry AD. Alternatives to gadolinium-based metal chelates for magnetic resonance imaging. Chem Rev 2010; 110(5): 2960–3018.
22. Sherry AD, Woods M. Chemical exchange saturation transfer contrast agents for magnetic resonance imaging. Annu Rev Biomed Eng 2008; 10: 391–411.
23. Baechle D, Cansier A, Fischer R, Brandenburg J, Burster T, Driessen C, Kalbacher H. Biotinylated fluorescent peptide substrates for the sensitive and specific determination of cathepsin D activity. J Pept Sci 2005; 11(3): 166–174.
24. Wender PA, Mitchell DJ, Pattabiraman K, Pelkey ET, Steinman L, Rothbard JB. The design, synthesis, and evaluation of molecules that enable or enhance cellular uptake: peptoid molecular transporters. Proc Natl Acad Sci USA 2000; 97(24): 13003–13008.
25. Vinogradov E, He H, Lubag A, Balschi JA, Sherry AD, Lenkinski RE. MRI detection of paramagnetic chemical exchange effects in mice kidneys in vivo. Magn Reson Med 2007; 58(4): 650–655.
26. Le WD, Xie WJ, Kong R, Appel SH. Beta-amyloid-induced neurotoxiity of a hybrid septal cell line associated with increased tau phosphoylation and expression of beta-amyloid precuror protein. J Neurochem 1997; 69(3): 978–985.
27. Jankowsky JL, Slunt HH, Ratovitski T, Jenkins NA, Copeland NG, Borchelt DR. Co-expression of multiple transgenes in mouse CNS: a comparison of strategies. Biomol Eng 2001; 17(6): 157–165.
28. Reiserer RS, Harrison FE, Syverud DC, McDonald MP. Impaired spatial learning in the APPSwe + PSEN1DeltaE9 bigenic mouse model of Alzheimer's disease. Genes Brain Behav 2007; 6(1): 54–65.
29. D'Andrea MR, Reiser PA, Polkovitch DA, Gumula NA, Branchide B, Hertzog BM, Schmidheiser D, Belkowski S, Gastard MC, Andrade-Gordon P. The use of formic acid to embellish amyloid plaque detection in Alzheimer's disease tissues misguides key observations. Neurosci Lett 2003; 342(1–2): 114–118.
30. Caravan P, Farrar CT, Frullano L, Uppal R. Influence of molecular parameters and increasing magnetic field strength on relaxivity of gadolinium- and manganese-based T1 contrast agents. Contrast Media Mol Imag 2009; 4(2): 89–100.
31. Nieminen MT, Rieppo J, Silvennoinen J, Toyras J, Hakumaki JM, Hyttinen MM, Helminen HJ, Jurvelin JS. Spatial assessment of articular cartilage proteoglycans with Gd-DTPA-enhanced T1 imaging. Magn Reson Med 2002; 48(4): 640–648.
32. Endres PJ, MacRenaris KW, Vogt S, Meade TJ. Cell-permeable MR contrast agents with increased intracellular retention. Bioconjugate Chem 2008; 19(10): 2049–2059.
33. Korb JP, Diakova G, Goddard Y, Bryant RG. Relaxation of protons by radicals in rotationally immobilized proteins. J Magn Reson Imag 2007; 186(2): 176–181.
34. Lopiano L, Fasano M, Giraudo S, Digilio G, Koenig SH, Torre E, Bergamasco B, Aime S. Nuclear magnetic relaxation dispersion profiles of substantia nigra pars compacta in Parkinson's disease patients are consistent with protein aggregation. Neurochem Int 2000; 37: 331–336.
35. Laurent S, Elst LV, Muller RN. Comparative study of the physicochemical properties of six clinical low molecular weight gadolinium contrast agents. Contrast Media Mol Imag 2006; 1(3): 128–137.
36. Strijkers GJ, Mulder WJM, van Heeswijk RB, Frederik PM, Bomans P, Magusin PCMM, Nicolay K. Relaxivity of liposomal paramagnetic MRI contrast agents. MAGMA 2005; 18: 186–192.
37. Aime S, Delli Castelli D, Geninatti Crich S, Gianolio E, Terreno E. Pushing the sensitivity envelope of lanthanide-based magnetic resonance imaging (MRI) contrast agents for molecular imaging applications. Acc Chem Res 2009; 42(7): 822–831.
38. Bernstein HG, Wiederanders B. An immunohistochemical study of cathepsin E in Alzheimer-type dementia brains. Brain Res 1994; 667: 287–290.
39. Aime S, Cabella C, Colombatto S, Geninatti CS, Gianolio E, Maggioni F. Insights into the use of paramagnetic Gd(III) complexes in MR-molecular imaging investigations. J Magn Reson Imag 2002; 16(4): 394–406.
40. Klunk WE, Engler H, Nordberg A, Wang Y, Blomqvist G, Holt DP, Bergstrom M, Savitcheva I, Huang GF, Estrada S, Ausen B, Debnath ML, Barletta J, Price JC, Sandell J, Lopresti BJ, Wall A, Koivisto P, Antoni G, Mathis CA, Langstrom B. Imaging brain amyloid in Alzheimer's disease with Pittsburgh Compound-B. Ann Neurol 2004; 55(3):306–319.
41. Clark CM, Schneider JA, Bedell BJ, Beach TG, Bilker WB, Mintun MA, Pontecorvo MJ, Hefti F, Carpenter AP, Flitter ML, Krautkramer MJ, Kung HF, Coleman RE, Doraiswamy PM, Fleisher AS, Sabbagh MN, Sadowsky CH, Reiman EP, Zehntner SP, Skovronsky DM. Use of florbetapir-PET for imaging beta-amyloid pathology. JAMA 2011; 305(3): 275–283.
42. Barthel H, Gertz HJ, Dresel S, Peters O, Bartenstein P, Buerger K, Hiemeyer F, Wittemer-Rump SM, Seibyl J, Reininger C, Sabri O. Cerebral amyloid-beta PET with florbetaben (18 F) in patients with

Alzheimer's disease and healthy controls: a multicentre phase 2 diagnostic study. Lancet Neurol 2011; 10(5): 424–435.
43. Jack CR, Jr, Lowe VJ, Weigand SD, Wiste HJ, Senjem ML, Knopman DS, Shiung MM, Gunter JL, Boeve BF, Kemp BJ, Weiner M, Petersen RC. Serial PIB and MRI in normal, mild cognitive impairment and Alzheimer's disease: implications for sequence of pathological events in Alzheimer's disease. Brain 2009; 132(Pt 5): 1355–1365.
44. Lopresti BJ, Klunk WE, Mathis CA, Hoge JA, Ziolko SK, Lu X, Meltzer CC, Schimmel K, Tsopelas ND, DeKosky ST, Price JC. Simplified quantification of Pittsburgh Compound B amyloid imaging PET studies: a comparative analysis. J Nucl Med 2005; 46(12): 1959–1972.
45. Mormino EC, Kluth JT, Madison CM, Rabinovici GD, Baker SL, Miller BL, Koeppe RA, Mathis CA, Weiner MW, Jagust WJ. Episodic memory loss is related to hippocampal-mediated beta-amyloid deposition in elderly subjects. Brain 2009; 132(Pt 5): 1310–1323.
46. Naslund J, Haroutunian V, Mohs R, Davis KL, Davies P, Greengard P, Buxbaum JD. Correlation between elevated levels of amyloid beta-peptide in the brain and cognitive decline. JAMA 2000; 283(12): 1571–1577.
47. Lue LF, Kuo YM, Roher AE, Brachova L, Shen Y, Sue L, Beach T, Kurth JH, Rydel RE, Rogers J. Soluble amyloid beta peptide concentration as a predictor of synaptic change in Alzheimer's disease. Am J Pathol 1999; 155(3): 853–862.
48. Walsh DM, Selkoe DJ. A beta oligomers – a decade of discovery. J Neurochem 2007; 101(5): 1172–1184.
49. Ropele S, Seifert T, Enzinger C, Fazekas F. Method for quantitative imaging of the macromolecular 1 H fraction in tissues. Magn Reson Med 2003; 49(5): 864–871.
50. Hammond DN, Lee HJ, Tonsgard JH, Wainer BH. Development and characterization of clonal cell lines derived from septal cholinergic neurons. Brain Res 1990; 512(2): 190–200.
51. Barbosa J, Jr, Massensini AR, Santos MS, Meireles SI, Gomez RS, Gomez MV, Romano-Silva MA, Prado VF, Prado MA. Expression of the vesicular acetylcholine transporter, proteins involved in exocytosis, and functional calcium signaling in varicosities and soma of a murine septal cell line. J Neurochem 1999; 73(5): 1881–1893.
52. Kushmerick C, Romano-Silva MA, Gomez MV, Prado MA. Changes in Ca(2+) channel expression upon differentiation of SN56 cholinergic cells. Brain Res 2001; 916(1–2): 199–210.
53. Blusztajn JK, Venturini A, Jackson DA, Lee HJ, Wainer BH. Acetylcholine synthesis and release is enhanced by dibutyryl cyclic AMP in a neuronal cell line derived from mouse septum. J Neurosci 1992; 12(3): 793–799.
54. Lorenzen A, Samosh J, Vandewark K, Anborgh PH, Seah C, Magalhaes AC, Cregan SP, Ferguson SS, Pasternak SH. Rapid and direct transport of cell surface APP to the lysosome defines a novel selective pathway. Mol Brain 2010; 3: 11.

